Physica E 81 (2016) 281–289

Contents lists available at ScienceDirect

Physica E

journal homepage: www.elsevier.com/locate/physe

ZnS/PVA nanocomposites for nonlinear optical applications

K. Ozga [a], J. Michel [b], B.D. Nechyporuk [c], J. Ebothé [b], I.V. Kityk [a,*], A.A. Albassam [d], A.M. El-Naggar [d,e], A.O. Fedorchuk [f]

[a] Institute of Electronics and Control System, Faculty of Electrical Engineering, Czestochowa University of Technology, Al. Armii Krajowej 17, Czestochowa 42-200, Poland
[b] Laboratory of Nanosciences Research (LRN), E.A. n°4682, UFR Sciences, Department of Physics, University of Reims Champagne Ardenne, 21 rue Clément Ader, 51685 Cedex 02, France
[c] Rivne State Humanitarian University, 31 Ostafova Str., Rivne 33028, Ukraine
[d] Research Chair of Exploitation of Renewable Energy Applications in Saudi Arabia, Physics and Astronomy Department, College of Science, King Saud University, P.O. Box 2455, Riyadh 11451, Saudi Arabia
[e] Physics Department, Faculty of Science, Ain Sham University, Abbasia, Cairo 11566, Egypt
[f] Department of Inorganic and Organic Chemistry, Lviv National University of Veterinary Medicine and Biotechnologies, 50 Pekarska Str., 79010 Lviv, Ukraine

HIGHLIGHTS

- Photoinduced nonlinear optics for ZnS/PVA nanocomposites is studied.
- Te aggregation does not play principal role in the SHG and TPA.
- The sizes define all the photoinduced optical properties.

ARTICLE INFO

Article history:
Received 24 February 2016
Received in revised form
18 March 2016
Accepted 21 March 2016
Available online 24 March 2016

Keywords:
Nanostructures
Electrochemical techniques
Optical properties
Transport properties

ABSTRACT

We have found a correlation between ZnS nanocomposite nonlinear optical features and technological processing using electrolytic method. In the earlier researches this factor was neglected. However, it may open a new stage for operation by photovoltaic features of the well known semiconductors within a wide range of magnitudes. The titled nanostructured zinc sulfide (ZnS) was synthesized by electrolytic method. The obtained ZnS nano-crystallites possessed nano-particles sizes varying within 1.6 nm… 1.8 nm. The titled samples were analyzed by XRD, HR-TEM, STEM, and nonlinear optical methods such as photo-induced two-photon absorption (TPA) and second harmonic generation (SHG). For this reason the nano-powders were embedded into the photopolymer poly(vinyl) alcohol (PVA) matrices. Role of aggregation in the mentioned properties is discussed. Possible origin of the such correlations are discussed.

1. Introduction

In the last decades, the study of novel composites based on semiconductor nano-crystals has attracted extensive scientific and industrial interests due to their strong size-dependent properties defining exceptional electronic and optical features [1–4]. Fabrication and characterization of these II – VI nanostructured semiconductors are recent area of enhanced scientific interest. Zinc sulfide (ZnS) is one of the most important group II–VI semiconductor with a wide band gap about 3.7 eV at ambient temperature with many excellent chemical and physical properties, which has promising applications in a lot of technical fields including photo-luminescence [5,6], electro-luminescence [7], nonlinear optical devices and fast optical switches [8,9]. Tables 1a, 1b, 2a, 2b.

It is well known that the ZnS nano-particles are promising for non-linear optics [10,11]. However, there is still a problem of obtaining the samples with sizes below 3 nm where simultaneously exists good long-range ordering and local interface disorder. There are different technological approaches to obtain the low-dimensional ZnS nano-crystallites, particularly by chemical method using PVP (polyvinylpyrrolidone) as a capping agent in aqueous solution [12,13] under ultrasonic radiation [14], by high-temperature chemical route [15] and other. However, the main restraining factor is a complicated methodology and bad reproducibility of the technology. At the same time it is important to obtain the nano-crystallites which may be operated by external laser light [16–18].

* Corresponding author.
E-mail address: iwank74@gmail.com (I.V. Kityk).

http://dx.doi.org/10.1016/j.physe.2016.03.041
1386-9477/

Table 1a
Theoretical (t) and experimental (e) data for different crystallographic planes which were used for evaluations of the structure; Δ – deviation parameter.

crystallographic parameters		*h k l*	*2-theta (e)*	*2-theta (t)*	*Δ*
space group	$P6_3mc$	0 1 0	31.864	31.879	−0.015
a (Å)	3.2520(4)	0 0 2	34.568	34.556	0.012
c (Å)	5.206(1)	0 1 1	36.374	36.365	0.008
radiation source	CuK_α	0 1 2	47.642	47.651	−0.009
wavelength	1.540562	1 1 0	56.678	56.674	0.003
LD	0.30(2)	0 1 3	62.964	62.965	−0.001
		0 2 0	66.442	66.440	0.002
		1 1 2	68.026	68.025	0.001
		0 2 1	69.148	69.150	−0.002

Table 1b
Parameters *2-theta* for *h k l* and interlayer distance *d* evaluated from experiment.

h k l	*2-theta*	*d*
0 1 0	31.959	2.79808
0 0 2	34.102	2.62695
0 1 1	36.347	2.469674
0 1 2	47.432	1.915176
1 1 0	56.955	1.615472
0 1 3	62.515	1.484503
0 2 0	66.814	1.39904
1 1 2	68.079	1.37609
0 2 1	69.468	1.351929
0 0 4	71.811	1.313475
0 2 2	77.187	1.234837
0 1 4	80.759	1.188991
0 2 3	89.610	1.093075
1 2 0	93.496	1.057575
1 2 1	95.968	1.036779
1 1 4	98.195	1.019127

Table 2a
The same as in the Table 1a for the Fig. 2.

crystallographic parameters		*h k l*	*2-theta (e)*	*2-theta (t)*	*Δ*
space group	$P6_3mc$	0 1 0	31.891	31.887	0.004
a (Å)	3.251(1)	0 0 2	34.597	34.592	0.005
c (Å)	5.201(3)	0 1 1	36.393	36.381	0.012
radiation source	CuK_α	0 1 2	47.677	47.684	−0.007
wavelength	1.540562	1 1 0	56.686	56.688	−0.002
LD	0.30(7)	0 1 3	63.006	63.019	−0.014
		0 2 0	66.427	66.457	−0.029
		1 1 2	68.086	68.059	0.027
		0 2 1	69.184	69.172	0.013

Table 2b
The same as in the Table 1b for *2-theta* axis.

h k l	*2-theta*	*d*
0 1 0	31.891	2.803879
0 0 2	34.597	2.5905
0 1 1	36.404	2.465925
0 1 2	47.761	1.902729
1 1 0	56.827	1.61882
0 1 3	63.180	1.470454
0 2 0	66.657	1.401939
1 1 2	68.264	1.372814
0 2 1	69.389	1.353271
0 0 4	72.982	1.29525
0 2 2	77.327	1.232963
0 1 4	81.852	1.17585
0 2 3	90.094	1.08845
1 2 0	93.245	1.059767
1 2 1	95.786	1.038268
1 1 4	99.216	1.011361

From this point of view very promising may be relatively simple electrochemical method in order to obtain very low-dimensional nano-crystallites with sizes below 2 nm possessing high degree of size dispersion. One of the principal problem is to separate contribution from separate particles and of the grains caused by a some aggregation. We will try to resolve this problem following the analysis of the microscopic, structural and nonlinear optical data in the electrochemically synthesized ZnS nanoparticles.

In the present work we explore the such prepared ZnS nanoparticles embedded into the PVA photopolymers using photo-induced nonlinear optics. Earlier it was shown very promising applications of the such kind nano-particles as embedded into the different organic matrices including PVA [19–22]. The initial nanoparticles were controlled using XRD, STEM and RH-TEM methods. Particular interest presents the photoinduced SHG which allow to study macroscopically disordered materials. However, in the research situation we will additionally control the sizes of the aggregates which may play some role in their nonlinear optical properties.

In the Section 2 are presented experimental methods including sample preparation and photo-induced nonlinear optical methods preparation. Section 3 is devoted to presentation of the principal results of the structural parameters of the nano-pawders and their photo-induced nonlinear optical features, including two photon absorption and photo-induced second harmonic generation. The discussion of the results is presented.

2. Materials and methods

2.1. Sample preparation conditions

Nanostructured ZnS is obtained by the electrolytic method in a glass electrolyzer using zinc electrodes of 8 mm diameter and 200 mm height. The solution of sodium thiosulfate in distilled water of 12.5 g/l of 39.1 g/l concentration is used as electrolyte. The electrolyte temperature varies in different experiments from room to 100 °C. The experiment duration is 2 h, with the current density of 1.21×10^{-2} or 2.30×10^{-2} A/cm^2. Regulated stabilized direct current is used as a power source. Uniform identical use of each zinc electrode is ensured by reversing the current direction every 30 min. The obtained ZnS nano-crystallites are ranged between 1.6 and 1.8 nm. In the present study, 8 samples of different deposition electrolyte temperatures (T_d) are used for the sample formation, namely: Zn-23:3 h (T_d=23 °C) with longer time of process – 3 hours, Zn-23 (23 °C), Zn-60 (60 °C), Zn-75 (75 °C), Zn-85 (85 °C), Zn-90 (90 °C), Zn-94 (94 °C) and Zn-98 (98 °C).

Such prepared nano-powders are embedded in the poly(vinil) alcohol (PVA) photopolymers at lower temperatures [23] on quartz substrate using a spin-coating method similar to the one described in ref. [24]. The optimal content of the nano-powder in PVA matrix is equal to about 8% in weight units.

2.2. Technical analyses

After finishing the electrolysis, the electrolyte is filtered through filter paper. The obtained powder is washed with a 5-fold volume of distilled water. The samples are air-dried at room temperature. XRD is performed using a DRON 4–13 X-ray diffractometer with CuK_α radiation at room temperature. Anode voltage and current are 41 kV and 21 mA, respectively. The scan step of the diffraction patterns is 0.05°, with 5 s exposure in each point.

Microscopy analyses of the as-prepared ZnS powder are performed in a dual acquisition mode using a JEOL 2100 F system

operating as a scanning Transmission Electron Microscope (STEM) and a high resolution Transmission Electron Microsccopy (HR-TEM). This system is used under a 200 kV voltage. The STEM micrographs are obtained with an electron probe of 1 nm size. They are recorded from an annular dark field detector (Gatan Ltd). The HR-TEM images are recorded from a GIF quantum CCD sensor. The system is also equipped with an energy dispersive X-ray spectrometer (EDS), the related spectra being recorded with a JEOL SDD detector.

The samples are measured by SHG in the PVA photo solidified films at different dc-electric fields. The dc-electric field is applied similarly to the method described in the ref. [25]. The fundamental laser beam is formed by a 18 ns Nd: YAG laser with a frequency of about 10 Hz. The variation of the maximal power densities is performed with a Glann polarizer up to 1 GW/cm^2 and the photoinduced beams formed by additional doubled frequency signal. The photoinduced treatment is performed before the measurements of the output SHG using a green 532 nm interferometric filter. The two-photon absorption is measured by intensity dependent transparency using the 1064 nm Nd: YAG laser as fundamental beam and applying extrapolation method described in the ref. [26]. The performed nonlinear optical methods give information about the nano-powder surface morphology which contributes substantially to the output nonlinear optics.

3. Results and discussion

3.1. Evolution of the crystal lattice parameters

Zinc sulfide may crystallize in either cubic sphalerite structure (T_d^2) or hexagonal wurtzite structure (C_{6V}^3). Depending on the conditions, its color may vary from white to yellow-white. In our case, we obtained white powders.

Diffraction patterns of Fig. 1 correspond to the samples obtained in 2-hr experiment with a reversing of the *dc* direction every 30 min for the electrolyte temperature of 23 °C (a) and 98 °C (b) and the sodium thiosulfate concentration of 39.1 g/l. The obtained experimental patterns are decomposed into Gaussian oscillators. We have thus yielded the following information on the reflection parameters: angle 2θ, *FWHM* β (width of the reflection at half its height) and integral intensity.

The diffraction pattern in Fig. 1a features three wide reflections which indicate small sizes of the produced particles. The calculations using Wolf-Bragg formula $2d\ sin\theta = k\lambda$ determined that the reflections correspond to planes (111) (2θ=29.2°), (220) (2θ=48.7°), (311) (2θ=56.6°). This is typical of the cubic structure of the sphalerite type. Calculations of the diffraction pattern in Fig. 1b determined that the featured reflections are characteristic of zinc oxide from the planes with Miller indices (100), (002), (101), (102), (110), (103), (200), (112), (201) which correspond to 2θ angles 31.9°; 34.6°; 36.4°; 47.7°; 56.7°; 63.0°; 66.5°; 68.1°; 69.2°, respectively. These correlate well with the data obtained in [27] on the investigation of zinc oxide nano-particles produced by electrolytic method. Additionally, Fig. 1b features low-intensity wide bands similar to those in Fig. 1a. Therefore, electrolyte temperature of 23 °C yields ZnS nano-crystals with the cubic structure, and a mixture of zinc oxide and sulfide are produced at 98 °C.

For more detailed reasons below is presented information concerning the principal structural parameters of the crystals. In the Table 1 are presented the evaluated parameters.

In Fig. 2 are given the same diffraction patterns (similarly to the Fig. 1) but for the samples prepared at the same conditions except the sodium thiosulfate concentration that is here equal to 12.5 g/l. Diffraction patterns show that the decrease of sodium thiosulfate concentration in the electrolyte to 12.5 g/l does not affect substantially the results. ZnS is still produced when the electrolyte temperature is 23 °C, and the mixture of ZnS and ZnO at 98 °C; but the relative intensity of ZnO reflections is higher than that of ZnS indicating higher content of zinc oxide in obtained powders.

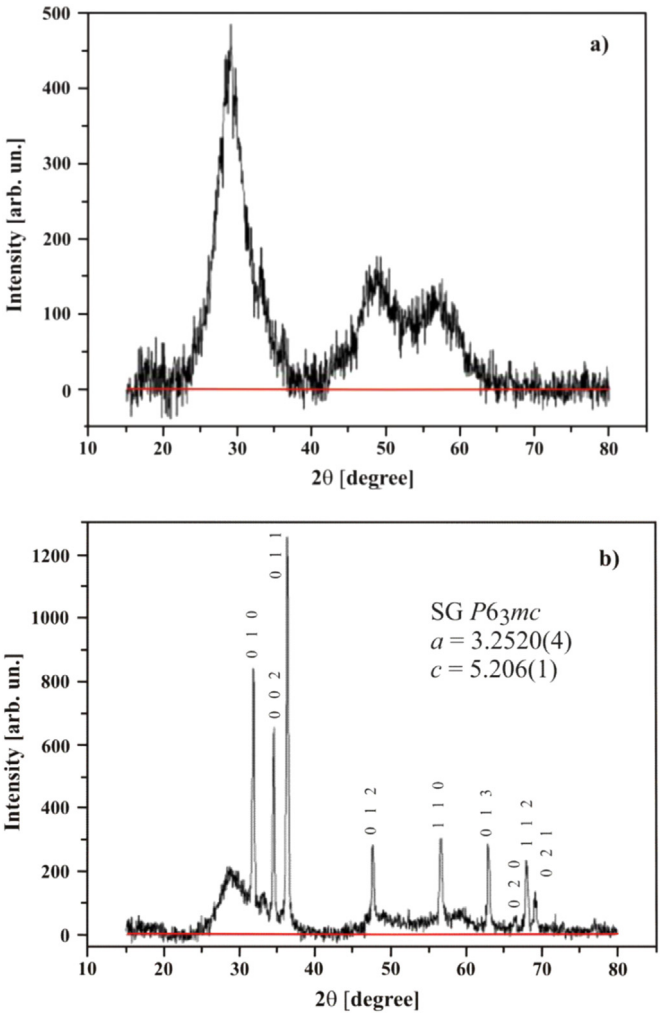

Fig. 1. X-ray diffraction patterns of samples produced at the electrolyte temperature 23 °C (a) and 98 °C (b) (sodium thiosulfate concentration was 39.1 g/l).

The size of obtained nano-particles of zinc oxide and sulfide is determined by X-ray structure analysis using Debye-Scherrer formula [28]:

$$D = \frac{k\lambda}{\beta \cos\theta} \quad (1)$$

where k is the particle shape coefficient (k=0.89); λ is the X-ray wavelength; β is the physical value of FWHM (full width at half maximum) of X-ray reflection; 2θ is the position of X-ray reflection.

The physical value of FWHM was calculated as:

$$\beta = \sqrt{\beta_1^2 - \beta_2^2} \quad (2)$$

where β_1 is the experimental value of FWHM of X-ray reflection; β_2 is the instrumental contribution to FWHM of X-ray reflection.

We have found a good agreement with compound PDF-4+ (ICDD) No 04-008-7254 [29] (see Fig. 2c).

The instrumental value of FWHM of X-ray reflections was determined from the analysis of the diffraction patterns of the standards, the powders of silicon and Al_2O_3, that were recorded under the same conditions. The calculations show that different reflections yield different results, and their average values are on

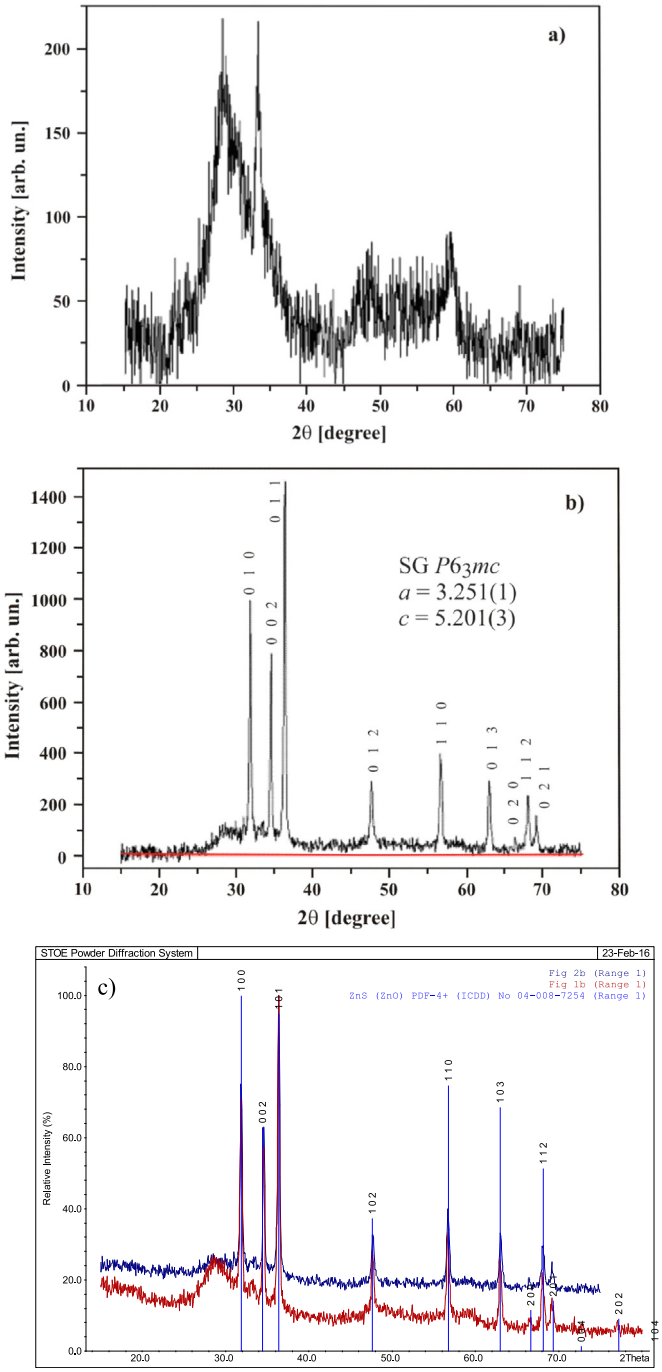

Fig. 2. X-ray diffraction patterns of samples produced at the electrolyte temperature 23 °C (a) and 98 °C (b) (sodium thiosulfate concentration was 12.5 g/l). (**c**) Comparison of the XRD spectra with the reference compounds.

the order 1.8 nm for zinc sulfide (Fig. 1a), and 1.6 nm for zinc sulfide and 38 nm for zinc oxide (Fig. 1b). A presence of sharp peak in XRD indicates on an additional aggregation of the ZnS nanoparticles into the grains.

An assumption was made that the FWHM value is affected, in addition to the size effect, by the defects of the crystal structure which produce mechanical strains. These are described by the formula [30]:

$$\varepsilon = \frac{\beta}{4tg\theta} \tag{2a}$$

where ε is the relative deformation; β is the physical value of FWHM.

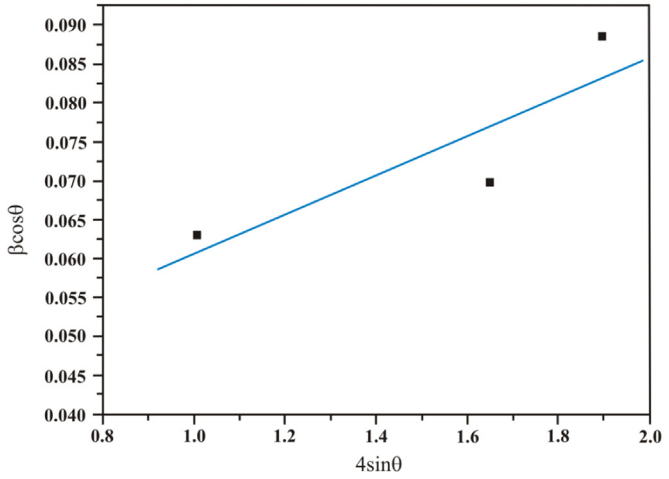

Fig. 3. Typical Williamson-Hall analysis of size effect and mechanical strain in zinc sulfide sample Zn-4 shown in Fig. 1a.

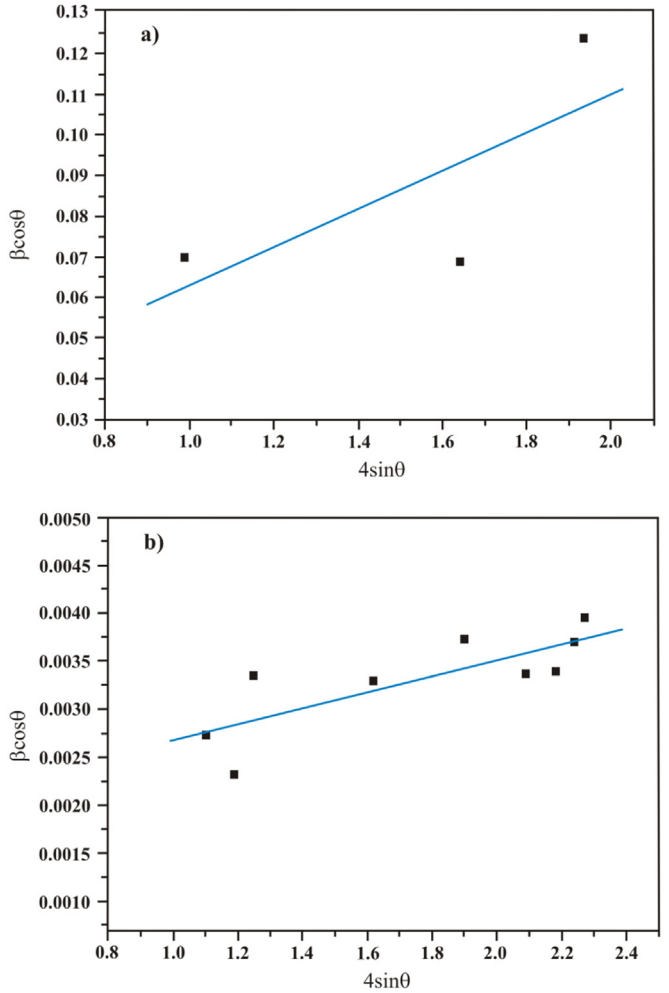

Fig. 4. Williamson-Hall analysis of size effect and mechanical strain in the sample the diffraction pattern of which is shown in Fig. 1b: a – ZnS, b – ZnO.

Therefore the physical value of FWHM, in case if both factors are active, is described as:

$$\beta = \frac{k\lambda}{D\cos\theta} + 4\varepsilon \cdot tg\theta \tag{3}$$

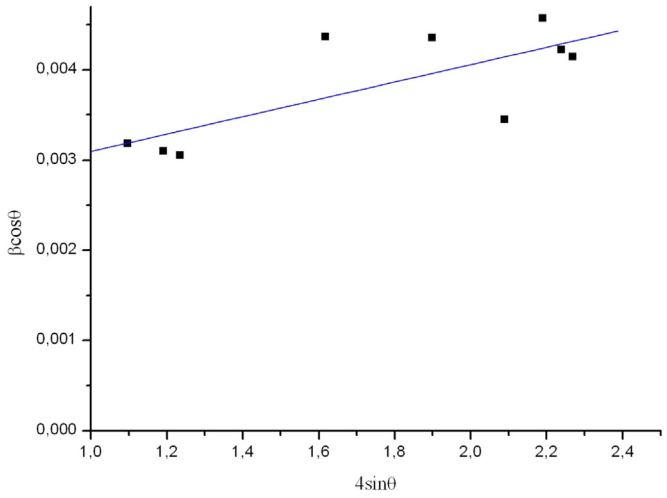

Fig. 5. Williamson-Hall analysis of size effect and mechanical strain in zinc oxide sample Zn-8 shown in Fig. 2b.

Williamson-Hall analysis [3] that is based on Eq. (3) is used to separate the two factors that affect the FWHM value. Eq. (3) is modified as:

$$\beta \cos\theta = \varepsilon 4 \sin\theta + \frac{k\lambda}{D} \tag{4}$$

and this dependence is viewed in coordinates ($4\sin\theta$, $\beta\cos\theta$). Clearly, such a choice of coordinates makes Eq. (4) into a linear function. Therefore, the values of D and ε may be determined from reliable experimental data using, for instance, least-squares method [31].

The results of Williamson-Hall analysis of zinc sulfide (diffraction pattern in Fig. 1a) that was obtained by the electrolytic method at 23 °C and electrolyte concentration of 39.1 g/l are presented in Fig. 3. A spread of experimental points around a line may be seen. Least-squares calculations yield the following values of $D=3.9$ nm, $\varepsilon=0.025$. The angular coefficient of the line is positive which indicates the presence of stretching strains in the sample.

The results of Williamson-Hall analysis of zinc sulfide and zinc oxide sample that was obtained similarly to the previous case at 98 °C and electrolyte concentration of 39.1 g/l are shown in Fig. 4. The least-squares calculations have given the following magnitudes of $D=8.8$ nm, $\varepsilon=0.047$ for zinc sulfide and $D=75$ nm, $\varepsilon=0.00084$ for ZnO. Similar to the previous case the angular coefficient of the line is positive.

In the Fig. 5 are presented analogous results for zinc oxide powder at 98 °C and the electrolyte concentration of 12.5 g/l. The similar simulations have given the following values: $D=72$ nm and $\varepsilon=9.6\times10^{-4}$. The authors of [32] performed Williamson-Hall analysis of the samples of CdS obtained by chemical precipitation from cadmium salts and sodium sulfide. Their data indicate

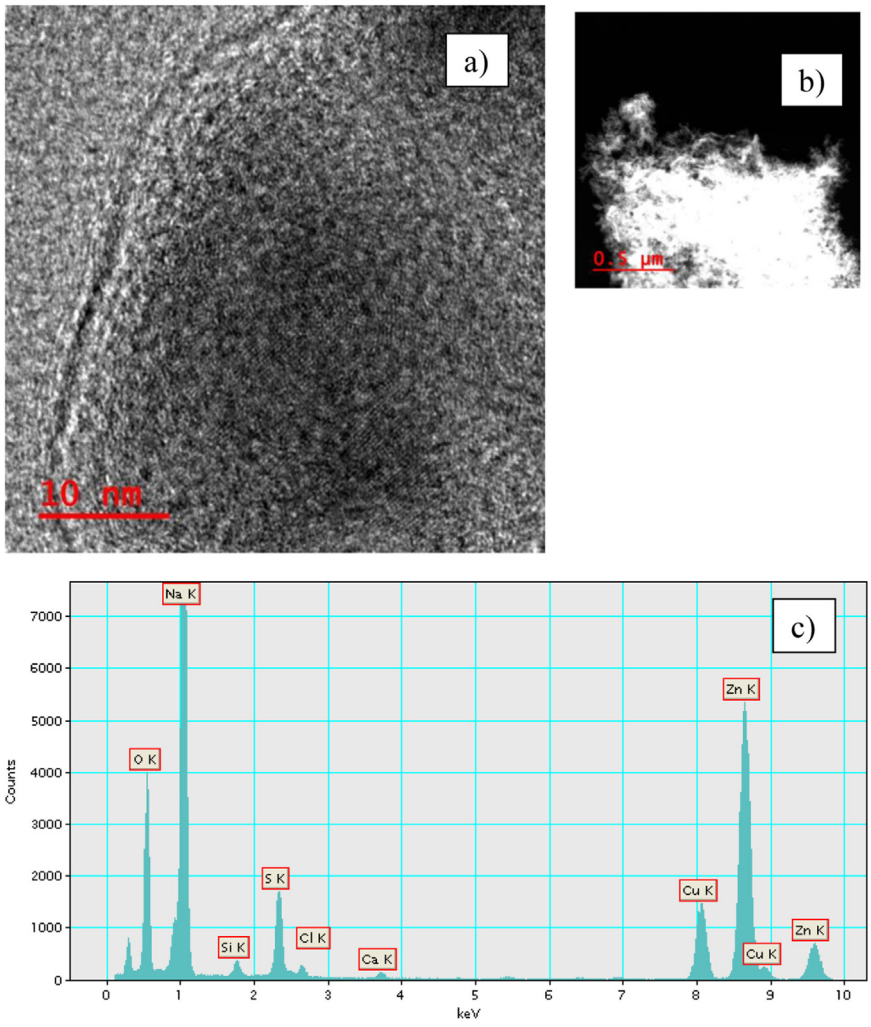

Fig. 6. Structural and compositional features of of ZnS samples obtained from electrolyte temperature 23 °C: a) HR-TEM micrograph; b) Dark field - STEM micrograph of the sample powder particle; c) EDS spectrum of the sample.

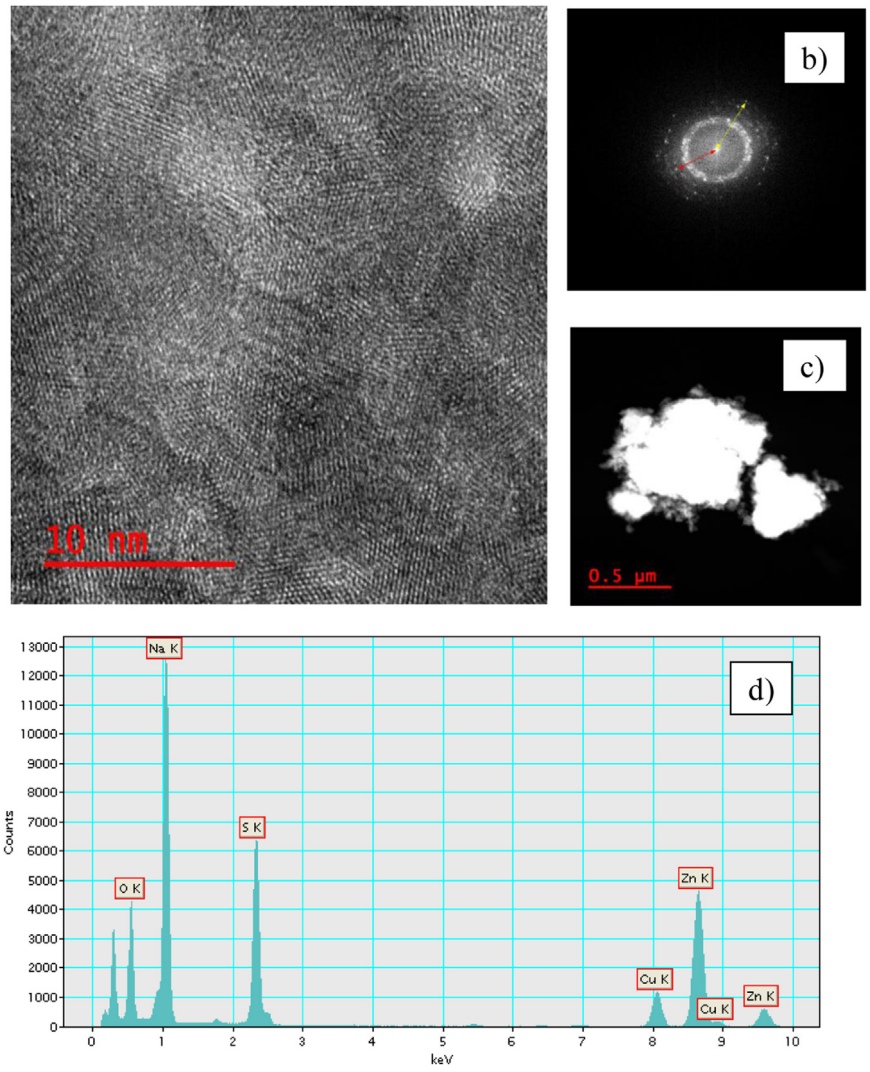

Fig. 7. Structural and compositional features of of ZnS samples obtained from electrolyte temperature 98 °C: a) HR-TEM micrograph; b) FTT diffractogram picture of the sample; c) Dark filed-STEM micrograph of the sample powder particle; d) EDS spectrum of the sample.

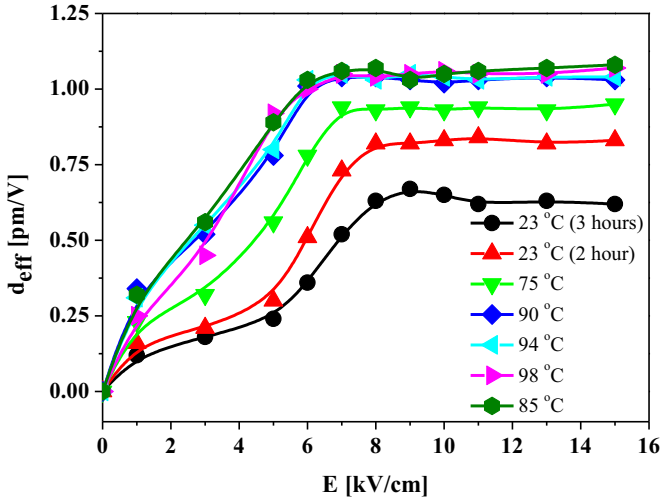

Fig. 8. Dependence of the SHG versus applied dc-electric field strength for the ZnS NP at different deposition electrolyte temperature T_d.

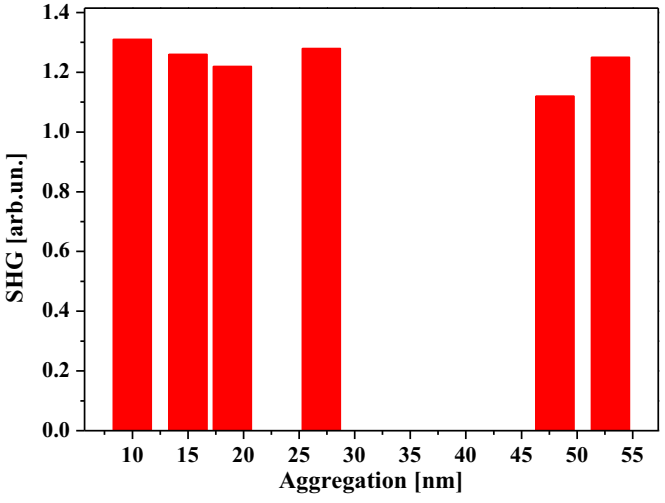

Fig. 9. Dependence of the SHG versus the aggregate sizes.

contracting strains (negative angular coefficient of the line). The investigation of zinc oxide obtained by chemical precipitation from the solutions of $Zn(CH_3COO)_2 \times 2H_2O$ and KOH in methanol at 52 °C produced the values of $D=35$ nm and $\varepsilon=0.00131$ [3]. In this case data indicate the stretching strains in the nano-particles (positive angular coefficient).

The study of the samples by transmission electron microscopy

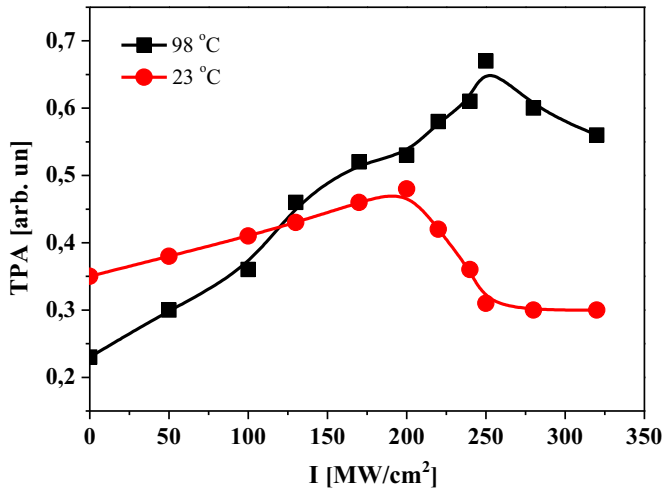

Fig. 10. Photoinduced TPA for the samples obtained at T_d=23 °C and 98 °C.

shows that their structural and compositional features are mainly affected by their deposition electrolyte temperature used during their formation stage (T_d). In actual fact, the differences observed in the results of the samples (Zn-23) and (Zn-23:3 h) respectively obtained after 2 and 3 hours at T_d=23 °C appeared very marginal. Although all of them are more or less crystallized, the degree of the crystalline feature is increasingly marked with the increase of T_d value. It is principal that following the data presented one can see clear coexistence of the low-dimensional nano-structures (about few nanometers) and higher grains formed by the nano-crystallites.

Fig. 6 reports the characteristics of the sample obtained at T_d=23 °C (Zn-23) while those of sample (Zn-98) obtained at T_d=98 °C are proposed in Fig. 7. The micrographs of the dark field-STEM proposed in Figs. 6b and 7c clearly show that the powder particles of the sample obtained at T_d=23 °C (Zn-23) are less condensed than those obtained at T_d=98 °C (Zn-98).

A more refined examination of the particles by HR-TEM analysis highlights the microstructure differences due to T_d values of each sample. It can be observed that the lattice orientations of the sample (Zn-98) obtained at T_d=98 °C are more defined in the micrograph of Fig. 7a than those of Fig. 6a related to the sample (Zn-23) obtained at T_d=23 °C. These TEM observations concur quite well with the results of the X-ray diffractograms of Figs. 1 and 2 proposed above for which the main peaks of this material correspond to the higher electrolyte temperature.

It can be also deduced from the HR-TEM micrograph of Fig. 7a that sample (Zn-98) corresponding to T_d=98 °C exhibits a real polycrystalline form since the related image depicts various orientations of the unit lattice which is clearly represented in the FTT micrograph of Fig. 7b. The results of the samples obtained at T_d=23 °C (Zn-98 and Zn-23) are less convincing in this particular aspect since the material crystallization seems incomplete.

The chemical analysis of the samples by EDS technique as proposed in Figs. 6c and 7d indicate the presence of some common impurities like Ca, Cl and Na in ZnS spectra. They might be the residues of the precursor materials used for the electrolyte preparation. Some side impurities like Cu come from the holder grid of the TEM while Si is likely to result from the glass substrate material.

A comparison of both EDS spectra indicates that the main peaks of Zn and S elements are present in both considered samples. However, it can be seen in Fig. 7d that the qualitative ratio of S element in the sample obtained at T_d=98 °C is clearly higher than the one of O element. The opposite situation is obtained in Fig. 6c related to the sample obtained at T_d=23 °C. Although a quantitative analysis remains necessary for accurate measurements, it can be deduced that ZnS material is mainly obtained at T_d=98 °C while ZnO is predominant in the sample obtained at T_d=23 °C. In any case, the presence of both materials concurs with the results of X-ray diffractommetry of some samples.

3.2. Nonlinear optical properties

The dependences of the SHG output efficiency of ZnS NP incorporated into PVA matrices has been investigated versus dc-electric for the samples synthesized at different deposition electrolyte temperature T_d. The results of Fig. 8 show that the optimal content of ZnS NP in the PVA corresponds to nearly 8% in weight units. The main increase of the effective SHG signal is obtained from the dc-electric field higher than 0.8 kV/cm, regardless of the sample considered. The saturation of the output susceptibilities observed afterwards is a consequence of the formation of the macroscopically aligned materials depicted by substantial enhancement of the second-order susceptibilities. This result concurs quite well with the formation of the acentric grating and the occurrence of the saturation processes. It is also clearly shown that the maximal SHG is only achieved for the electrolytic treatments T_d=85 °C. Further increase or decrease of T_d from that value leads to less d_{eff} magnitudes. Here the main role begins to play an interaction between the photopolarized alignment and the disordering factor destroying the alignment. Some role also may play the ZnS NP aggregations which occur during the embedding process. The output SHG is degraded after 48 hours up to 30% with respect to initial maxima.

To evaluate a role of aggregations we have chosen the composites with different effective aggregate sizes and studied their SHG. The nano-crystals which were embedded were separated

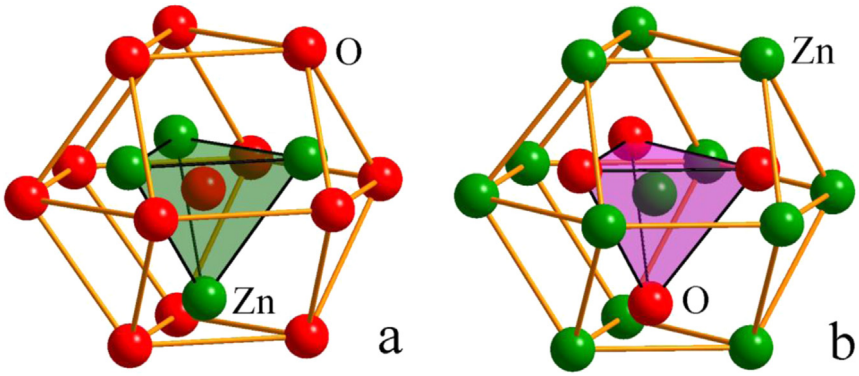

Fig. 11. Second anion coordination of oxygen atoms (a) and second coordination of Zn atoms (b) for ZnO structural type.

following the TEM method of the polymer nanocomposites as described in the ref. [33]. The corresponding results are presented in the Fig. 9 for the nano-particle with the same sizes. One can see that there is not observed an evident correlation with the size of aggregates contrary to the nano-particle sizes. The size dispersion did not exceed 13%.

It is well known that the nonlinear optical hyperpolarizabilities directly related to the corresponding hyperpolarizabilities. The polarizability of the nano-particles during treatment by electromagnetic field possesses two terms: linear P_i^L and non-linear P_i^{NL}:

$$\vec{P}_i = \vec{P}_i^{\,L} + \vec{P}_i^{\,NL} = \alpha_{ij}E_j^{(\omega)} + \beta_{ijk}E_j^{(\omega)}E_k^{(\omega)} + \gamma_{ijkl}E_j^{(\omega)}E_k^{(\omega)}E_l^{(\omega)}\vec{P}_i^{\,L}$$
$$= \alpha_{ij}E_j^{(\omega)}\vec{P}_i^{\,NL} = \alpha_{ij}E_j^{(\omega)} + \beta_{ijk}E_j^{(\omega)}E_k^{(\omega)} + \gamma_{ijkl}E_j^{(\omega)}E_k^{(\omega)}E_l^{(\omega)} \quad (5)$$

Here α_{ij}, β_{ijk} and γ_{ijkl} are hyperpolarizabilites which define macroscopic susceptibility χ_{ijk} by equations:

$$\chi_{ij}^{(\omega)} = \alpha_{ij}L_i^{(\omega)}L_j^{(\omega)},\ \chi_{ijk}^{(\omega)} = \beta_{ijk}L_i^{(\omega)}L_j^{(\omega)}L_k^{(\omega)},\ \chi_{ijkl}^{(\omega)} = \gamma_{ijkl}L_i^{(\omega)}L_j^{(\omega)}L_k^{(\omega)}L_l^{(\omega)} \quad (6)$$

where *i, j, k* are Cartesian components of the local Lorenz electrostatic field described by $L_{i,j,k}$. In the semi-empirical approach the microscopic hyperpolarizabilities can be presented as:

$$\alpha_{ij} \cong \frac{\vec{\mu}_i\vec{\mu}_j}{E_g^2},\ \beta_{ijk} \cong \frac{\vec{\mu}_i\vec{\mu}_j\Delta\vec{\mu}_k}{E_g^3},\ \gamma_{ijkl} \cong \frac{\vec{\mu}_i\vec{\mu}_j\Delta\vec{\mu}_k\Delta\vec{\mu}_l}{E_g^4} \quad (7)$$

where $\vec{\mu}_{i,j}$ are transition matrix dipole moments and $\Delta\vec{\mu}_{k,l} = \Delta\vec{\mu}_{k,l}^{(ex)} - \Delta\vec{\mu}_{k,l}^{(gr)}$ are principal differences between excited and ground dipole moments.

The dipole moment vector possesses two principal part: electronic and phonon: $\vec{\mu} = \vec{\mu}_{el} - \vec{\mu}_{ph}$, where $\vec{\mu}_{el}$: is electronic dipole moment being less dependent versus temperature and $\vec{\mu}_{ph}$: is dipole momentum's phonon part of which is sensitive to temperature and related anharmonic electron-phonon interactions. Such interactions are determined by the third-order space derivatives of the anharmonic potentials:

$$\gamma_{ijkl} = \frac{\partial^3 U}{\partial x_i \partial x_j \partial x_k} \quad (8)$$

which is expressed in a form:

$$U = \frac{1}{2!}\alpha_{ij}x^2 - \frac{1}{3!}\beta_{ijk}x^3 - \frac{1}{4!}\gamma_{ijkl}x^4 \quad (9)$$

where *U* represents the total electrostatic potential. The second and third terms determine the anharmonic interaction. For the study of the nano-crystallites, we should consider three main parts which are: the long-range ordered crystallites, the interfaces and the surrounding amorphous-like background.

The calculations are performed by the norm-conserving pseudo-potential method as described in the ref. [34] where it is shown that the dipole moments of the interfaces are almost one order higher compared to the long-range ordered and amorphous like states. So the nano-interfaces will here play main role.

To evaluate the influence of the structures on the nano-crystallites optical properties, we have performed the study of the photo-induced TPA using a simple intensity dependent method [35] the photo- induction being performed similarly to the one described in the ref. [36].

The illumination was done by the bicolor 1064 nm/532 nm laser as described in the ref. [37] (see some examples in the Fig. 10). One can see that the pump powered dependence is substantially opposite. For the sample obtained at electrolyte temperature 98 °C we observe a maximum and for the sample at 23 °C after less maximum about 190 MW/cm^2 one can see a huge decrease at 250 MW/cm^2. It may reflect a different feature of the samples versus the external light and a competition between the polarization and the thermal effects.

Following the ref. [38–40] s anion coordination [41] of the oxygen atoms for the atoms in the structural types of ZnO may be presented in a form of hexagonal analogous of cubooctahedra, where Zn atoms occupy half of tetrahedral voids as shown in the Fig. 11a. At the same time yet 6 voids remain unoccupied. For the second cationic coordination of Zn atoms, the features of coordination polyhedral remain unchanged (see Fig. 11b). A similar situation is considered for the shape and sizes of voids by the oxygen atoms. For ZnS nano-particles, the situation is the same than for the wurtzite-like structure. The presented data unambiguously show that despite existence of aggregates, the grains formed by the low-dimensional nanostructures do not play the crucial role in the observed photoinduced SHG.

The discovery of principal role of the microscopic structure of nano-crystallites in the NLO is shown. Such finding may be used for design of novel polymer nanocomposites.

4. Conclusions

For the first time we have established a substantial enhancement of the photo-induced second and third order susceptibilities of the nanostructured zinc sulfide (ZnS) crystallites synthesized by electrolytic method. Contrary to the previous work where such an influence was as a rule neglected we have shown a possibility of operation by optical and nonlinear optical susceptibility in wide range of magnitudes which also is important for photovoltaic operations. The presented data unambiguously show that, despite the existence of the aggregates, the grains formed by the low-dimensional nanostrcutures do not play a crucial role in the observed photo-indcued SHG. The optimal achieved SHG is observed at 85 °C electrolytic treatments. Further increase deposition electrolyte temperature leads to less d_{eff} magnitudes. The output SHG is degraded up to 30% after 48 hours with respect to initial maxima. Additionally, we have found a substantially opposite dependence of the TPA.

Conflict of interests

None

Acknowledgments

The project was financially supported by King Saud University, Vice Deanship of research chairs. Authors J. Michel and J. Ebothe acknowledge the technical support from the PICT IBiSA imaging center of University of Reims Champagne Ardenne (France).

References

[1] H. Kumar, P.B. Barman, R.R. Singh, Physica E 60 (2015) 168–177.
[2] C. Burda, X. Chen, R. Narayanan, A. El-Sayed, Chem. Rev. 105 (4) (2005) 1025–1102.
[3] C.B. Murray, C.R. Kagan, M.G. Bawendi, Annu. Rev. Mater. Sci. 30 (2000) 545–610.
[4] L. Chen, C. Wang, Q. Li, S. Yang, L. Hou, S. Chen, J. Mater. Sci. 44 (2009) 3413–3419.
[5] A.R. Loukanov, C.D. Dushkin, K.I. Papazova, A.V. Kirov, M.V. Abrashev, E. Adach, Colloid Surface 245 (1-3) (2004) 9–14.
[6] S.V. Svechnikov, L.V. Zavyalova, N.N. Roshchina, V.E. Rodionov, V. S. Khomchenko, L.I. Berezhinskii, et al., Semiconductors 34 (2000) 1128–1132.
[7] K. Manzoor, S. Vadera, N. Kumar, T. Kutty, Appl. Phys. Lett. 84 (2004) 284–286.
[8] D. Jassby, M. Wiesner, Langmuir 27 (3) (2011) 902–908.

[9] M.Q. Israr, J.R. Sadaf, L.L. Yang, O. Nur, M. Willander, J. Palisaitis, et al., Appl. Phys. Lett. 95 (2009) 073114.
[10] Z. Dehghani, S. Nazerdeylami, E. Saievar-Iranizad, M.H.M. Ara, J. Phys. Chem. Solids. 72 (9) (2011) 1008–1010.
[11] R.A. Ganeev, M. Baba, M. Merita, D. Rau, H. Furii, A.I. Ryasnyansky, N. Ishizawa, M. Suzuki, H. Kuroda, J. Opt. A: Pure. Appl. Opt. 6 (2004) 447.
[12] S. Nazerdeylami, E. Saievar-Iranizad, Z. Dehghani, M. Molami, Physica B 406 (2011) 108–111.
[13] Z. Jindal, N.K. Verma, J. Mater. Sci. 43 (2008) 6539–6545.
[14] J.F. Xu, W. Ji, J.Y. Lin, S.H. Tang, Y.W. Du, App. Phys. A 66 (6) (1998) 639–641.
[15] V.V. Nikesh, A. Dharmadhikari, H. Ono, S. Nozaki, G.R. Kumar, S. Mahamuni, Appl. Phys. Lett. 84 (2004) 4602.
[16] D. Rajesh, T. Sarkar, A. Mulchandani, Appl. Phys. Lett. 99 (2011) 173110.
[17] T. Yatsui, F. Morigaki, T. Kawazoe, Beilstein. J. Nanotechnol. 14 (5) (2014) 1767–1773.
[18] F. Ramtolli, G. Saccinni, Cryst. Res. Technol. 37 (12) (2002) 1325–1330.
[19] S.S. Talwatkar, Y.S. Tamgadge, A.L. Sunatkari, A.B. Gambhire, G.G. Muley, Solid State Sci. 38 (2014) 42–48.
[20] Y.S. Tamgadge, A.L. Sunatkari, S.S. Talwatkar, V.G. Pahurkar, G.G. Muley, Opt. Mater. 37 (2014) 42–50.
[21] S.S. Talwatkar, A.L. Sunatkari, Y.S. Tamgadge, V.G. Pahurkar, G.G. Muley, Appl. Phys. A 118 (2) (2014) 675–682.
[22] Y.S. Tamgadge, S.S. Talwatkar, A.L. Sunatkari, V.G. Pahurkar, G.G. Muley, Thin Solid Films 595 (2015) 48–55.
[23] I.V. Kityk, J. Kasperczyk, B. Sahraoui, M.F. Yasinskii, B. Holan, Polymer 38 (19) (1997) 4803–4806.
[24] K. Danel, K. Ozga, I.V. Kityk, Chem. Phys. 313 (1-3) (2005) 33–38.
[25] I.V. Kityk, R.I. Mervinskii, J. Kasperczyk, S. Joasi, Mater. Lett. 27 (4-5) (1996) 233–237.
[26] M.C. Rumi, J.W. Perry, Adv. Opt. Photonics 2 (2010) 451–518.
[27] M.K. Balakirev, I.V. Kityk, V.A. Smirnov, L.I. Vostrikova, J. Ebothe, Phys. Rev. A 67 (2003) 023806.
[28] V.R. Gayevskyi, B.D. Nechyporuk, M.Y. Novoselytskyi, B.P. Rudyk, Ukr. Phys. J. 58 (2013) 388–391.
[29] E.H. Kisi, M.M. Elcombe, Acta Crystallogr. C 45 (1989) 1867–187.
[30] R.P. Pawar, Orient. J. Chem. 29 (2013) 1139–1142.
[31] V.D. Mote, Y. Purushotham, B.N. Dole, J. Theor. Appl. Phys. 66 (2012) 1–8.
[32] C. Lawson, R. Hanson, Numerical solutions using least-squares method, Nauka, Moscow, 1986.
[33] S. Tkaczyk, M. Galceran, S. Kret, M.C. Pujol, M. Aguilo, F. Diaz, A.H. Reshak, I. V. Kityk, Acta Mater. 56 (2008) 5677–5684.
[34] I.V. Kityk, A. Kassiba, K.J. Plucinski, J. Berdowski, Phys. Lett. A. 265 (2000) 403–410.
[35] J. Ebothe, I.V. Kityk, I. Fuks-Janczarek, Appl. Surf. Sci. 252 (2006) (5763–576).
[36] M.K. Balakirev, V.A. Smirnov, L.I. Vostrikova, I.V. Kityk, J. Kasperczyk, W. Gruhn, J. Mod. Opt. 50 (2003) 1237–1244.
[37] R.P. Prabhu RR, M.A. Khadar, Bull. Mater. Sci. 31 (3) (2008) 511–515.
[38] A. Douayar, M. Abd-Lefdil, K. Nouneh, P. Prieto, R. Diaz, A.O. Fedorchuk, I. V. Kityk, Appl. Phys. B 110 (2013) 419–423.
[39] M. Abd-Lefdil, A. Douayar, A. Belayachi, A.H. Reshak, O.A. Fedorchuk, S. Pramodini, P. Poornesh, K.K. Nagaraja, H.S. Nagaraja, J. Alloy Compd. (2014) 7–12.
[40] M. Abd-Lefdil, A. Belayachi, S. Pramodini, P. Poornesh, A. Wojciechowski, A. O. Fedorchuk, Laser Phys. 24 (2014) 035404 (7pp).
[41] A.O. Fedorchuk, O.V. Parasyuk, I.V. Kityk, Mater. Chem. Phys. 139 (2013) 92–99.